JET–P(97)53

Transport in JET Deuterium Plasmas with Optimised Shear*

G A Cottrell, Y Baranov, D O'Brien, C D Challis, J G Cordey, J C M de Haas[1], L-G Eriksson, C Gormezano, A C Howman, T C Luce[2], M Mantsinen[3], G J Sadler, A C C Sips, F X Söldner, D F H Start, P M Stubberfield, B J T Tubbing, D J Ward, M von Hellermann, W P Zwingmann.

JET Joint Undertaking, Abingdon, Oxfordshire, OX14 3EA,
[1] Netherlands Foundation for Research in Astronomy, Dwingeloo, NL.
[2] General Atomics, San Diego, California, USA.
[3] Also at Helsinki University of Technology, Association Euratom-TEKES, Espoo, Finland.

* Expanded version of a contributed paper presented at the 24th European Physical Society Conference on Controlled Fusion and Plasma Physics, Berchtesgaden, Germany, 1997. Proc. Volume 21A, Part1, p.81.

Preprint of a Paper to be submitted for publication in
Plasma Physics and Controlled Fusion

December 1997

"This document is intended for publication in the open literature. It is made available on the understanding that it may not be further circulated and extracts may not be published prior to publication of the original, without the consent of the Publications Officer, JET Joint Undertaking, Abingdon, Oxon, OX14 3EA, UK".

"Enquiries about Copyright and reproduction should be addressed to the Publications Officer, JET Joint Undertaking, Abingdon, Oxon, OX14 3EA".

ABSTRACT

Plasmas with the highest deuterium fusion neutron rates (R_{DD}= 5.6 × 10^{16} s^{-1}) yet achieved in JET have been produced by combining a hollow or flat central current profile with a high confinement (H-mode) edge. In these discharges, LHCD and ICRH preheating, applied early in the current ramp-up phase, 'freezes in' a hollow or flat current density profile. When the combined NBI and ICRH heating power is increased, a region of reduced transport and highly peaked profiles forms during the L-mode phase which persists into the later H-mode phase when the fusion reactivity reaches a maximum. Transport analysis shows the formation of a central region of good confinement (the internal transport barrier or ITB) which expands with radial velocity ~ 0.5 m s^{-1}. The clearest signatures of this region are large gradients in the ion temperature and toroidal rotation profiles. Ion thermal diffusivities in the central region are of the order of the neo-classical value. The position and rate of expansion of the ITB radius correlate well with the calculated rational q=2 surface. The confinement improvement can also be seen in electron density, and, to a lesser extent, in electron temperature, but not necessarily at the same radial region. The ITB can persist in combination with the edge transport barrier characteristics of the H-mode.

1. INTRODUCTION

One of the major efforts in research and development of thermonuclear fusion in tokamaks is the exploration of new regimes with improved confinement. Higher confinement implies a smaller (and therefore cheaper) fusion reactor. Improvements in performance can, in principle, be gained by increasing the central plasma pressure within the limits imposed by MHD stability. One well-known regime is the H-mode, in which a thermal transport barrier forms in a narrow radial region just inside the magnetic separatrix. In general, pressure profiles in H-mode discharges are broad with large gradients existing near the plasma edge. These steep edge gradients, allied with limitations on current density, can destabilise edge-localised MHD modes (ELMs) and outer MHD modes whilst, in the core, the rise in central plasma parameters is limited by sawteeth and other MHD activity.

Alternative improved regimes are based on increasing the particle and energy confinement in the centre of the plasma. Sawteeth can be avoided by operating the tokamak with a high value of the central safety factor, $q \geq 1$, a regime that can be accessed by applying additional heating during the current rise. Improved central confinement and high performance have been demonstrated on JET by central pellet fuelling of non-sawtoothing discharges combined with intense central heating [1]. The central magnetic shear ($s = r/q(\mathrm{d}q/\mathrm{d}r)$) in these discharges was low and negative - a condition that was found to be associated with improved central confinement [2]. More recently, other large tokamaks (TFTR [3], DIII-D [4] and JT60 [5]) have explored heating during the current rise and all have demonstrated improvements in the central

confinement and in fusion performance. When high power heating is applied to JET tokamak plasmas during the early current rise phase (the optimised shear regime), the central plasma confinement is also observed to improve - this occurs when the magnetic shear in a central region is close to zero [6,7,8]. Similar improvements have also been seen using LHCD. Optimised shear JET plasmas were prepared by preheating a low initial density plasma target; detailed operational aspects of these have been described in [9].

A summary example of a typical JET high performance optimised shear deuterium discharge is shown in Fig.1. This discharge, with toroidal field B_T = 3.8T, attained peak values of density ($n_{e0} = 6 \times 10^{19}$ m^{-3}), ion and electron temperatures (T_{i0} = 32 keV and T_{e0} =13 keV respectively) and DD neutron emission ($R_{DD} = 5.6 \times 10^{16}$ s^{-1}). In order to delay the current penetration to the core, two preheating phases were used. The early preheating phase used 1.1 MW of LHCD power from time t = 0.38 s to 1.2 s. This was followed by 1 MW of central ICRH preheating applied from time t = 2.88 s until the start of the main heating phase. The ICRH scheme was in

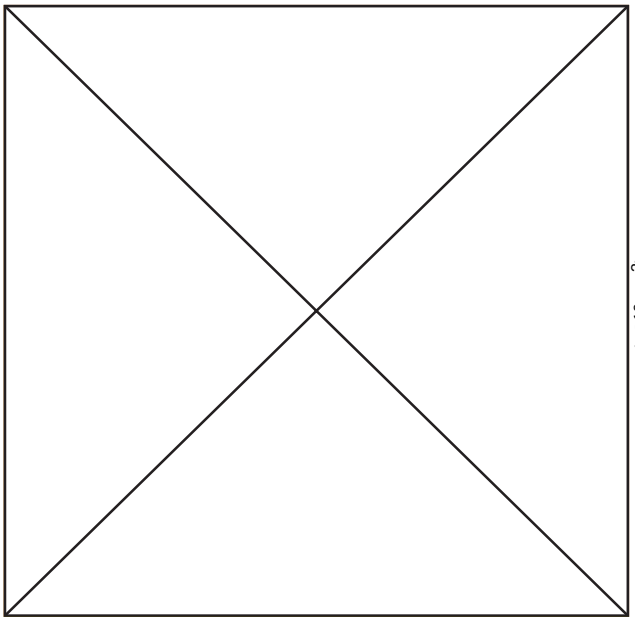

Fig.1.Overview of JET high performance optimised shear pulse No. 42426 showing the ramp-up phase of the plasma current (trace a*) during which combined deuterium neutral beam injection ($P_{NBI} \leq 17.5$ MW) and central ICRH ($P_{RF} \leq 6.0$ MW) was applied (trace* b*). Trace* c *shows that the diamagnetic stored energy reached a peak value of W_{dia}= 12.5 MJ at time 7 s. Traces* (c) *and* (d) *show the central values of electron density, ion and electron temperatures reach peak values of* $n_{e0} = 6 \times 10^{19}$ *m*$^{-3}$, T_{i0} = *32 keV and* T_{e0} =*13 keV. The total DD and DT neutron emission (trace* f*) reaches a maximum rate of* $R_{DD} + R_{DT} = 8.1 \times 10^{16}$ *s*$^{-1}$, *of which* $R_{DD} = 5.6 \times 10^{16}$ *s*$^{-1}$ *was from DD fusion reactions. The intensity of* D_α *emission is shown in trace* g.

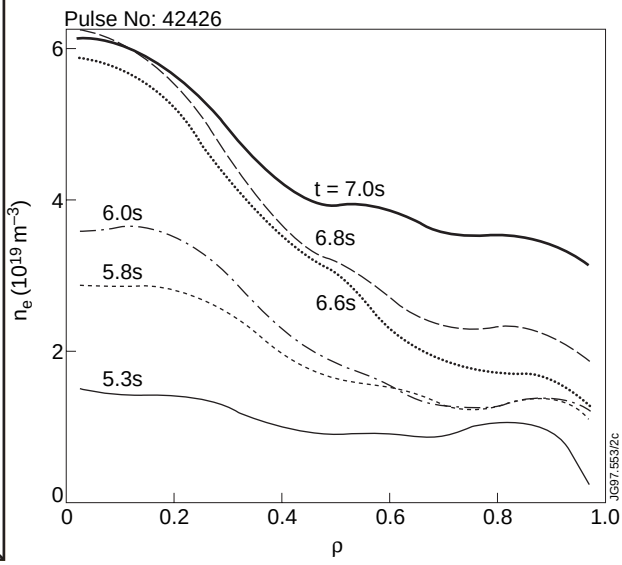

Fig.2. Evolution of LIDAR profiles of electron number density mapped onto the normalised radial co-ordinate, ρ*, with the TRANSP code equilibrium. Note the strong peaking of the density which occurred during the L-mode phase (time* t ≤*6.6 s) which persisted into the H-mode phase (time* t ≥ *6.68 s) at which time the density at the edge increased sharply.*

the hydrogen minority H(D) regime with central resonance. At time t = 5 s, when the plasma current was 2.4 MA, high power combined NBI and ICRF heating was applied. Some 8 MW of near radially-directed neutral beams were injected into the low density ($n_{e0} = 1.5 \times 10^{19}$ m^{-3}) target deuterium plasma (Fig. 2) and the ramp-up from 1 MW to 6 MW of ICRH power started.

As both plasma density and current increased, a bank of near tangentially-directed neutral beams was added; this gave a total NBI power of 17.5 MW combined with 6 MW of ICRH. At time $t \sim 5.6$ s there was a spontaneous transition to a state of improved central confinement - the birth of an internal transport barrier (ITB). Both the plasma density and current continued to increase with the current reaching its maximum flat-top value of 3.6 MA at time t = 7.0 s. The plasma remained in the L-mode until, at time t = 6.68 s, a decrease in D_α emission (Fig. 1) showed the formation of an ELM-free H-mode. The evolution of the ion temperature and plasma pressure profiles is shown in Figs. 3 and 4 respectively. The peaking of central plasma parameters increased progressively during the L-mode phase.

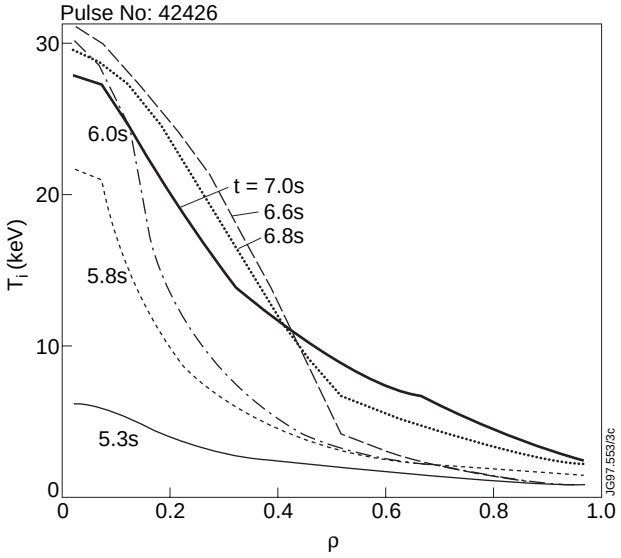

Fig.3. Evolution of the ion temperature profile (from charge-exchange recombination measurements) mapped onto the normalised radial co-ordinate, ρ, with the TRANSP code equilibrium. Note the early presence of a steep gradient region which expanded radially with time indicating the formation of a region of low transport (internal transport barrier).

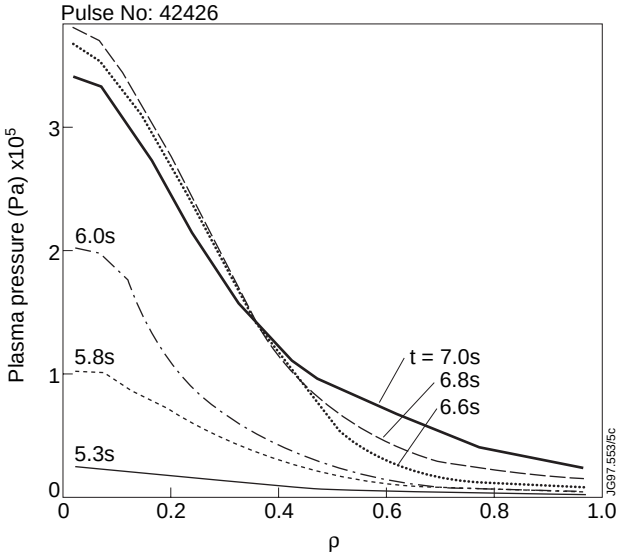

Fig.4. Evolution of the plasma pressure profile showing the formation of a steep gradient region that moved radially outwards with time during the L-mode phase. The maximum central pressure ($p_0 = 3.8 \times 10^5$ pa) was attained near the time of the LH transition (time t = 6.68 s) after which the inner ($\rho \leq 0.4$) pressure gradient decreased and the outer ($\rho \geq 0.4$) pressure gradient increased.

The central plasma parameters remained high during the ELM-free H-mode phase, but the rate of rise of the total 2.5 MeV DD neutron emission rate (Fig. 5) decreased at time t = 6.8 s (reaching a peak value of $R_{DD} = 5.6 \times 10^{16}$ neutrons s^{-1} at time t = 7.0 s). Although no tritium was introduced into this discharge, the plasma contained a small trace (~ 0.5%), originating from wall release following earlier operations with tritium. The measured component of the total neutron emission from 14 MeV DT fusion neutrons was $R_{DT} = 2.4 \times 10^{16}$ s^{-1}. The rate of rise of

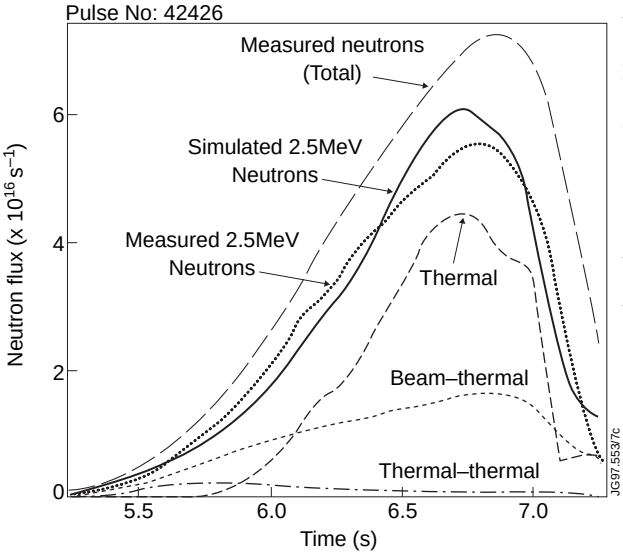

Fig.5. Measured and simulated neutron fluxes. The measured total includes 2.5 MeV DD and 14.7 MeV DT neutrons, the latter component arose from a residual trace tritium component in the plasma. The measured total 2.5 MeV DD neutron flux is compared with the TRANSP simulated 2.5 MeV DD neutron flux. Approximately 70% of the simulated total arose from thermal-thermal DD reactions with the remainder coming from beam-thermal and beam-beam reactions.

the diamagnetic stored energy also decreased, near the time of the H-mode transition, reaching a peak value of W_{dia} = 12.5 MJ at time t = 7.0 s. By this time the central electron density had reached $n_{e0} = 6 \times 10^{19}$ m^{-3}; the central electron temperature was T_{e0} = 13 keV and the central ion temperature was T_{i0} = 28 keV. Subsequently, the total neutron emission rate decreased and, at time t = 7.06 s, a giant ELM - as seen from the sharp increase in D_α emission - terminated the phase of improved confinement.

2. ANALYSIS AND DATA CONSISTENCY

For analysis we have used the TRANSP transport code [10, 11], to reconstruct JET optimised shear discharges. This code contains a magnetic equilibrium solver, Monte-Carlo models for the neutral particles, the injected beam ions and fusion ions that were tracked during their slowing-down history. The ICRF heating model is based on a full-wave solver coupled with a Fokker-Planck description of a minority fast ion distribution as well as direct (second harmonic) damping on bulk ions and transit-time magnetic-pumping (TTMP) and Landau damping on thermal electrons. The effect of the second harmonic interaction of ICRF with energetic beam ions was modelled and the RF power damped on energetic beam ions computed.

The primary input data to the TRANSP code are as follows. The bulk ion, minority ion and dominant impurity ion species were specified. The magnetic data used included the position of the plasma boundary, the total plasma current and toroidal field. The profile data for electron density was from LIDAR measurements (as in Fig. 2), and ion temperature, effective plasma charge and toroidal rotation velocity profiles were from active charge-exchange recombination measurements during the neutral beam injection phase (as in Fig.3). The total radiation loss, measured bolometrically, was also included. The electron temperature (from electron cyclotron emission measurements) was input as a function of frequency and then mapped, self-consistently, on to the radial co-ordinate using the TRANSP equilibrium solver.

This analysis was performed on a number of JET high performance optimised shear discharges including the example shown in Fig.1. The calculated total 2.5 MeV DD neutron rate (Fig. 5) lies within the estimated error of ± 10% of the measurement, with thermonuclear neutron emission comprising approximately 70% of the total and most of the remainder originating from beam-thermal DD reactions. The reasonable agreement between reconstructed and measured neutron rates indicates that any second harmonic ICRF/NBI interaction did not produce a significant deuterium tail. This result contrasts with some earlier optimised shear discharges [12], where the central electron density was lower and the RF interaction stronger. Comparison was also made between the calculated and measured line-of-sight integrated neutron emission profiles. The agreement between the horizontally viewing neutron camera data and reconstruction is reasonable (Fig. 6). Compared with data from the vertically viewing camera, the shape of the reconstructed profile is reasonable but there appears to be a small systematic outward radial displacement of the centroid of emission by ~ 5 cm. The centroid of soft X-ray emission (from a vertically viewing camera) was in agreement with the neutron camera data, confirming the outward radial displacement of the reconstructed position of the magnetic axis .

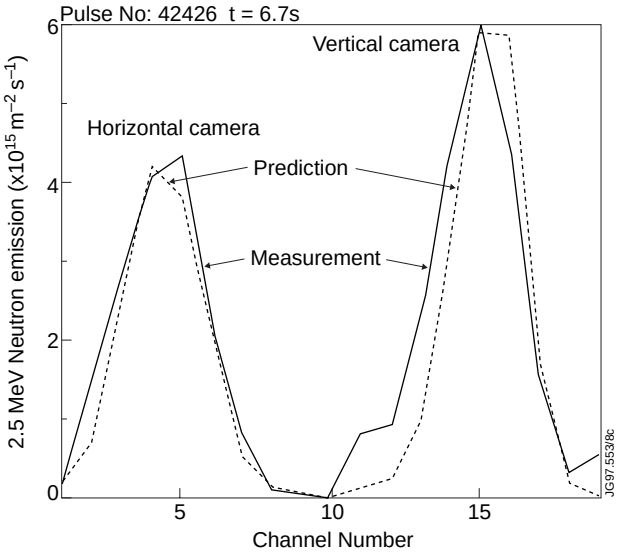

Fig.6. Comparison of TRANSP simulated collimated 2.5 MeV DD neutron emission rate with measured neutron collimator data. Channels 1-9 and 10-19 belong, respectively, to the horizontally and vertically viewing neutron collimators. In the mid-plane of the plasma the channel-to-channel separation corresponds to approximately 0.2 m.

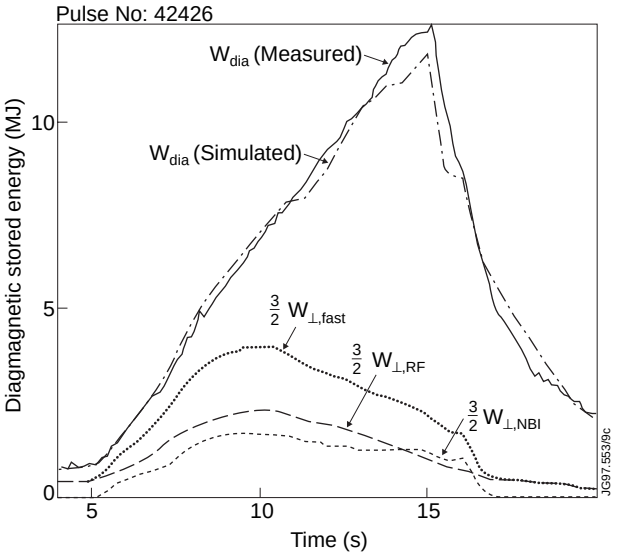

Fig.7. Comparison of measured and TRANSP-simulated diamagnetic energy content, showing the relative contributions to the stored energy from thermal, fast ICRF minority H ions and fast NBI D ions.

The total thermal energy content ($W_{thermal}$) and the perpendicular ion energy contents arising from ICRH and NBI fast ions ($W_{\perp,\,fast} = W_{\perp,\,RF} + W_{\perp,\,NBI}$) were computed and combined to give a reconstructed diamagnetic energy content ($W_{dia} = W_{thermal} + 1.5 \times W_{\perp,fast}$) which was compared with measurement (Fig. 7). The computed diamagnetic energy content agrees reasonably well with measurement, lying within the estimated experimental error band of ± 1 MJ. At the time of peak fusion performance,

fast ions contributed 21% to the diamagnetic signal. However, at the earlier time during the ITB growth phase t = 6.0 s, the fast ion component was larger, comprising 57% of the diamagnetic signal (of which 58% was in the form of fast H minority ions and 42% in the form of fast NBI deuterons).

2. SAFETY FACTOR AND CURRENT DENSITY PROFILES

The evolution of the plasma equilibrium was determined self-consistently in the TRANSP code by solving the Grad-Shafranov equation in conjunction with the measured kinetic pressure profiles and the computed fast ion pressure profiles. Current diffusion was calculated neo-classically. In the simulations presented here, the q-profile from EFIT reconstruction was used for the initial part of the TRANSP modelling up to time t = 4.5 s, just before the application of the main heating. Thereafter, with a change-over time of 0.5 s, there was a switch to the TRANSP calculation. As a check of the subsequent evolution, the TRANSP simulation showed that $q(0)$ had decreased to approximately unity by the time (t = 12.5 s) of the first appearance of sawteeth in the discharge. When the main additional heating was applied, the q-profile (Fig.8) increased monotonically with radius with $q \geq 2$ everywhere. At the time the ITB was born ($t \sim 5.5$ s), the q-profile flattened near $\rho = 0.4$ at a value just above 2 and subsequently became weakly inverted. By the time of maximum fusion performance (time t = 7.0 s), q had fallen below 2 everywhere inside $\rho = 0.55$ and showed a minimum value of approximately 1.9 at normalised radius $\rho \sim$ 0.43.

Fig.9 shows the composition of the total plasma current and its components computed using TRANSP. At time t = 5.7 s, shortly after the application of the main heating power, the

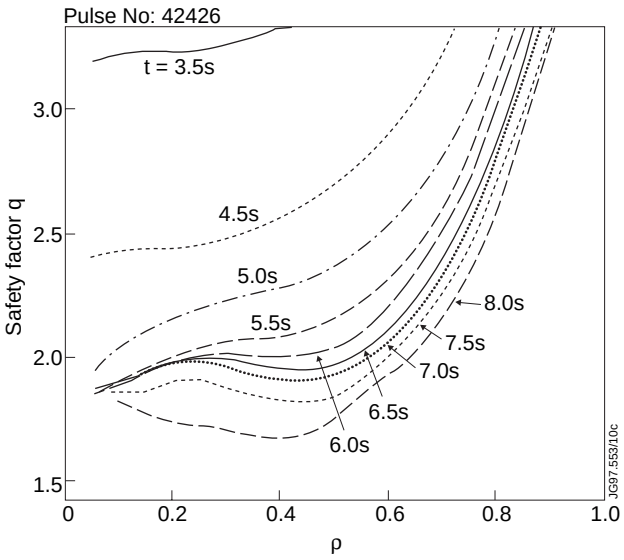

Fig.8. Evolution of the safety factor profile from combined TRANSP and EFIT reconstruction. This reconstruction shows the formation of a region of negative shear during the high performance (ITB) phase of the discharge.

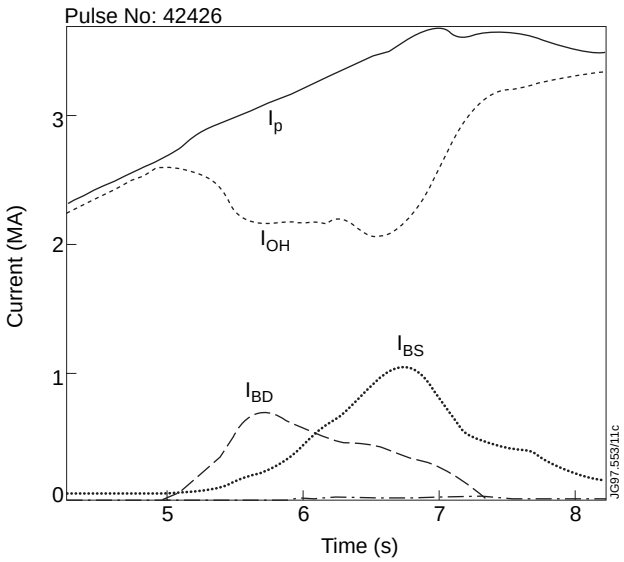

Fig.9. Composition of the total plasma current. Total current: I_p ; ohmic current: I_{OH}; beam-driven current : I_{BD}; and bootstrap current: I_{BS}.

beam-driven current was the most significant non-inductive component, carrying 23% of the total current. The current density profiles (Fig.10(a)) show the beam-driven current density peaking at ρ =0.22 causing a flattening of the total current density profile out to a radius ρ =0.4. As the central plasma density increased with time, the beam fast ion content and the beam-driven component decreased. The bootstrap current fraction increased significantly after the formation time of the ITB and, by the time of the H-mode transition (t = 6.68 s), had reached 30% of the total. At that time the beam-driven current and ohmic current fractions had decreased, respectively, to 10% and 60% of the total. During the ITB phase, at time t = 6.7 s, Fig. 10(b) shows the bootstrap current density peaking at ρ = 0.25 with the total current density having developed an off-axis peak at ρ = 0.4.

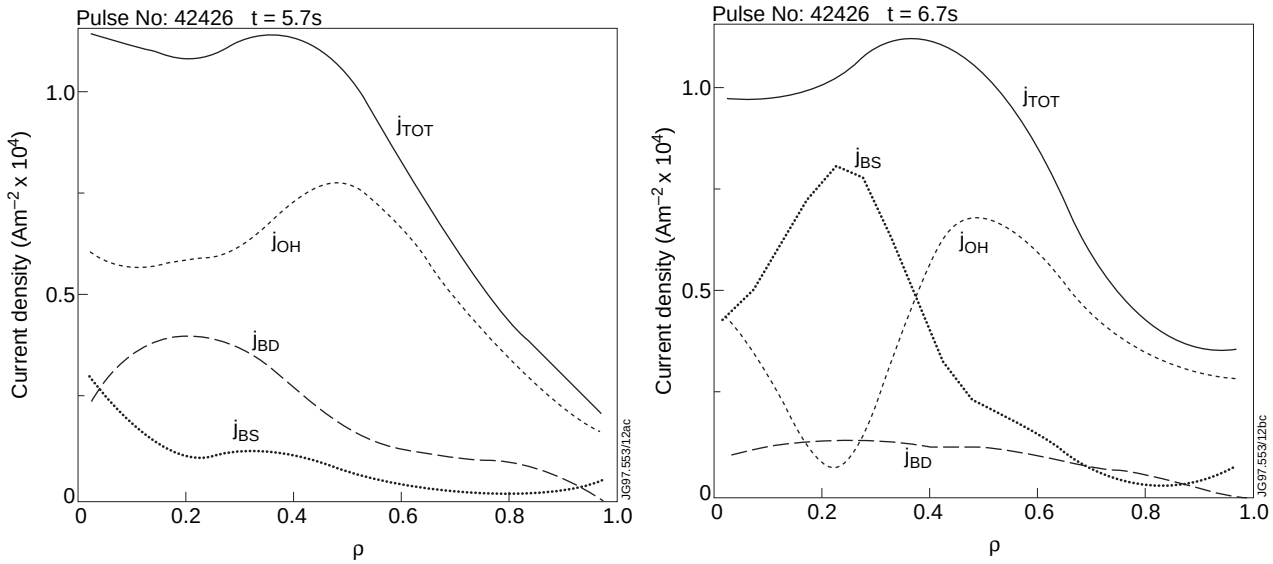

Fig.10. Current density profiles (a) at time t = *5.7 s and (b)* t = *6.7 s. Total current density: j_{TOT}, ohmic current density: j_{OH}, bootstrap current density: j_{BS}, and beam-driven current density: j_{BD}.*

3. HEATING PROFILES

ICRF heating with $\pi/2$ phasing and frequency f = 51.7 MHz was coupled to the plasma with the waveform P_{RF} (Fig. 11). It should be noted that the RF power was controlled in real time. The heating was at the fundamental hydrogen minority (H)D frequency with the second harmonic deuterium cyclotron resonance located close to the magnetic axis. The H minority concentration was measured to be 2.2% of the ion density. The power coupled to minority ions at fundamental resonance ($P_{RF,min}$) was initially a large fraction of P_{RF}. However, as the hot ion core formed, the central ion beta, $\beta_D(0)$, increased and an increasingly large fraction of power is calculated to be coupled directly to the thermal ions at second harmonic resonance ($P_{RF,i}$). The power coupled to fast injected beam deuterons ($P_{RF,NB}$) also increased, reaching a peak value at time t =5.8 s corresponding to the maximum density of fast injected deuterons. At the time of peak fusion performance (t = 7 s), $\beta_D(0)$ had increased to a level where $P_{RF,i}$ had become comparable with

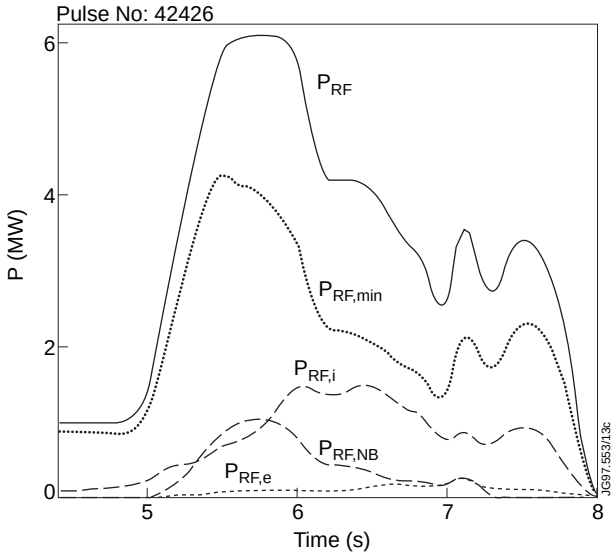

Fig.11. RF heating powers. P_{RF}: Total power coupled to the plasma; $P_{RF,min}$: RF power coupled to minority H ions at fundamental resonance; $P_{RF,i}$: RF power coupled to majority D ions at second harmonic resonance; $P_{RF,NB}$: RF power coupled to NBI D ions at second harmonic resonance; $P_{RF,e}$: RF power coupled to thermal electrons.

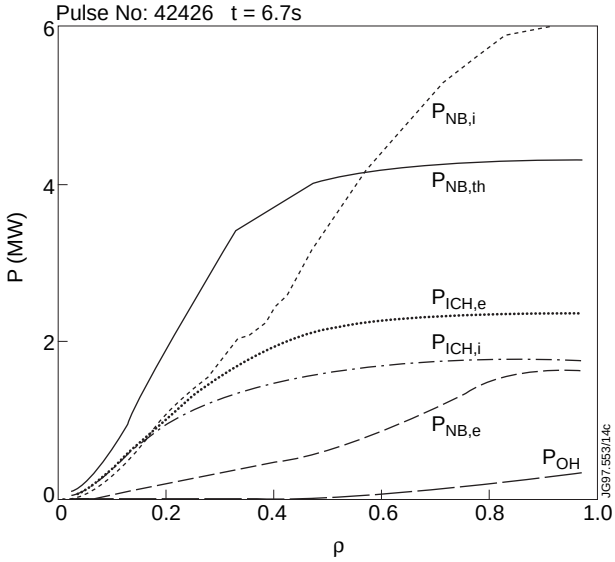

Fig.12. Profiles of volume-integrated heating power to ions and to electrons from ICRH and NBI. $P_{ICH,e}$: RF power deposited on electrons (comprising the sum of the direct TTMP/ELD and the redistributed power to electrons from the minority species); $P_{ICH,i}$: RF power deposited on ions (comprising the sum of the direct and the redistributed power to ions from the minority species); $P_{NB,i}$: NBI power deposited on ions; $P_{NB,\,th}$: thermalised NBI power (deposited on ions); $P_{NB,\,e}$: NBI power deposited on electrons; and P_{OH} : ohmic heating.

$P_{RF,min}$. The step-down in the ICRH power was used, operationally, as a control of the central pressure profile peaking in order to reduce the impact of high frequency MHD activity on barrier performance [9].

The TRANSP profiles of volume-integrated heating power to ions and electrons are shown in Fig. 12 at the time of the H-mode transition. The RF power deposition was centrally peaked with 38% (1.3 MW) of the coupled RF power heating ions and 47% (1.6 MW) heating electrons within ρ = 0.3. The remaining 15% was coupled to the injected beam ions. The NBI heating profile was broader than that of the ICRH. Shine-through NBI power losses decreased with time as the ITB grew: at t = 5.5 s the loss was 5.5 MW, decreasing to 1.4 MW at time t = 6.6 s. Charge-exchange beam loss was 2 MW at t = 5.5 s, decreasing to 1.0 MW at t = 6.5 s.

4. TRANSPORT

4.1 Energy Balance

In the L-mode phase with the well-formed ITB present, the main loss of heat from the plasma was through the ion channel (Fig. 13) with equipartition, convection and conduction comparable in the region $\rho \leq 0.4$ but conduction dominating losses at larger radii. Heat loss from the ions

to the electrons by equipartition was comparable (~ 2 MW) with the convective loss. In the electron channel (Fig. 14), equipartition electron heating was comparable with all other electron heating terms in the centre ($\rho \leq 0.4$). Conduction dominated the electron losses over most of the plasma column.

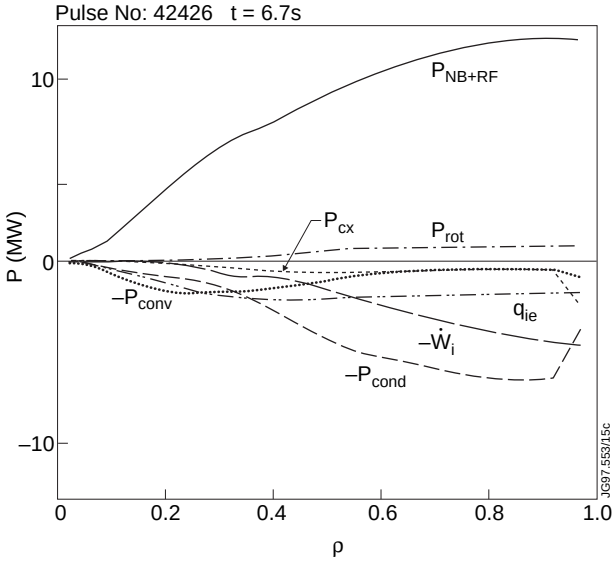

Fig.13. Ion energy balance (volume-integrated). P_{NB+RF}: Total ion heating power; P_{rot}: power to rotation ; $-P_{CX}$: power lost via charge-exchange collisions ; $-d/dt(W_i)$: power lost in changing the ion thermal energy content; $-P_{cond}$: power lost via conduction; $-P_{conv}$: power lost via convection.

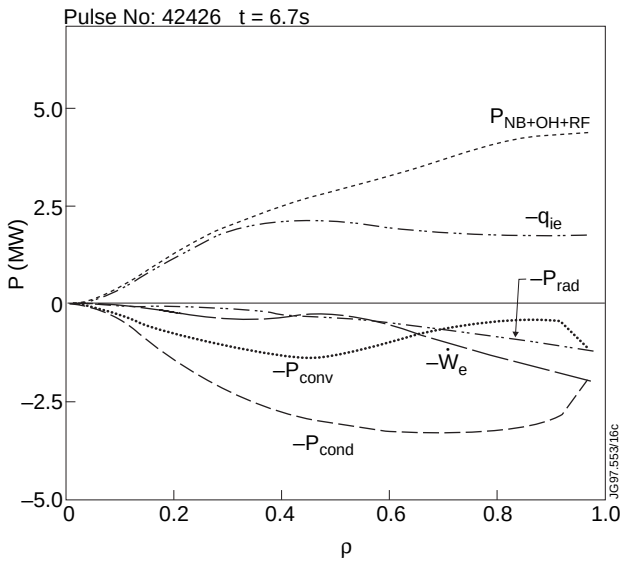

Fig.14. Electron energy balance (volume-integrated). $P_{NB+OH+RF}$: Total electron heating power; $-P_{rad}$: power loss via radiation; $-d/dt(W_e)$: power lost in changing the electron thermal energy content; $-P_{cond}$: power lost via conduction; $-P_{conv}$: power lost via convection.

4.2 Heat Transport

The presence of an internal transport barrier is most clearly revealed as a large reduction in the ion thermal diffusivity, χ_i, inside a central region that expands with time (Fig. 15). The angular momentum diffusivity, χ_ϕ, behaved similarly. The ion thermal diffusivity at $\rho = 0.1$ started to decrease at time t ≈5.3 s revealing the birth of the transport barrier in the centre of the plasma. The development of the ITB can be seen as a progressive radial expansion of the low diffusivity region. The χ_i and χ_ϕ barriers grew with radial velocity ~ 0.5 m s^{-1} for a time of ~ 1.4 s. When the H-mode edge barrier formed, the ITB had expanded to its maximum

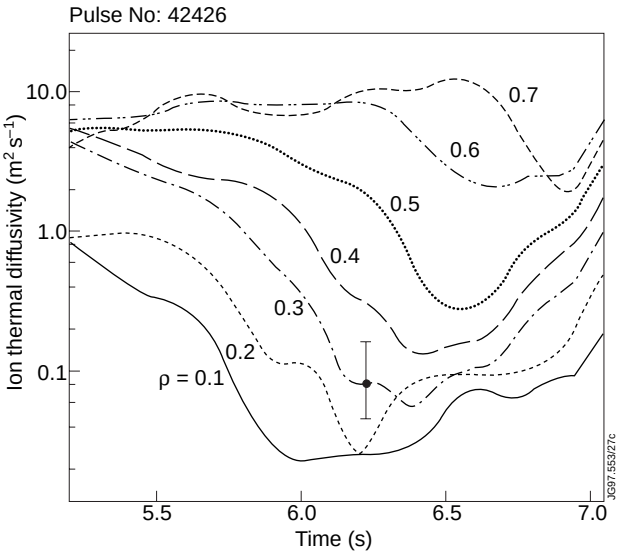

Fig.15. Loci of normalised radii, ρ , in the ion thermal diffusivity (χ_i) - time plane.

radius of $\rho \approx 0.55$ and, in the outer region of the plasma ($\rho \geq 0.7$), the ion thermal and angular momentum diffusivities decreased sharply leading to a transient phase of enhanced confinement over 80% of the plasma cross-section. However, just before the time of the L→ H transition, transport within the innermost radii ($\rho \leq 0.15$) had begun to increase showing that the barrier confinement had started to degrade progressively from the centre outwards. During the ELM-free period the diffusivities in the central region increased showing the continued degradation of the central confinement. After the large ELM the diffusivities at all radii had become comparable with their values in the early L-mode phase.

The radial profiles of χ_i before and during the internal transport barrier phase are shown in Fig. 16. At time 6.67 s, the profile is compared with the standard neo-classical expectation, $\chi_{i,neo}$. It can be seen that χ_i was comparable in magnitude with $\chi_{i,neo}$ in the radial range $\rho = 0.1 - 0.25$. The neo-classical calculation was made assuming the ion banana width to be small compared with typical length scales. However, owing to the high ion temperature and low value of poloidal field near the plasma centre, this comparison becomes increasingly uncertain as the centre is approached. As regards the improvements in electron thermal and particle diffusivity with the formation of the ITB, we have found that these transport coefficients can be reduced by typically a factor of two when there is a clear ITB signature in the ion channel.

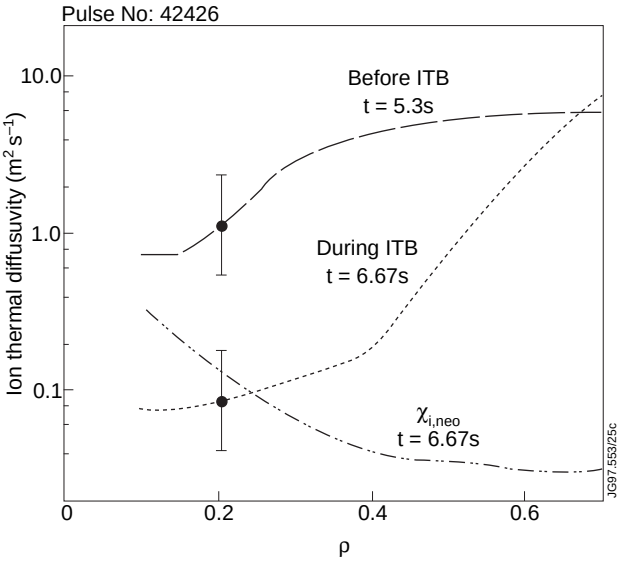

Fig.16. Profiles of ion thermal diffusivity (χ_i) before and during the ITB phase. The neo-classical expectation, $\chi_{i,neo}$ is shown for comparison.

4.3 Evolution of the Internal Transport Barrier

To identify the location of the transition from low to high transport regions, we have computed the second radial derivative of various quantities such as the ion temperature profile: $d^2 T_i / d\rho^2$ that has a maximum at the position of the'footpoint' of the ITB (Fig. 17). Using this definition, Fig. 18 shows the radii of the ITB footpoints of various quantities plotted together with the normalised radius of the q=2 rational surface. Up to the time of the H-mode, the radii of the ITB footpoints of ion thermal diffusivity, χ_i and angular momentum diffusivity, χ_f are reasonably well correlated (Fig. 19) with the calculated radius of the q=2 surface. Although the radius of the footprint of the electron density follows the growth curve of the other quantities, it is displaced outwards by approximately $\Delta\rho = 0.15$. When the H-mode appears, there is a sharp decrease in the radii of all ITB footpoints.

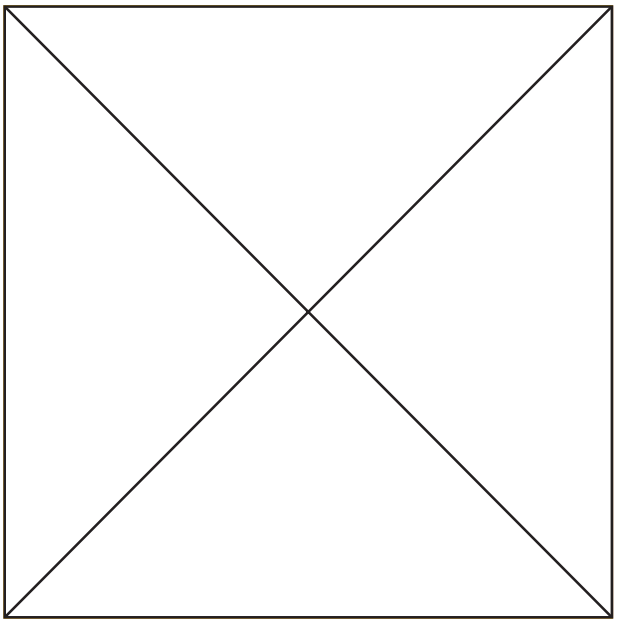

Fig.17. Contour plot of the second radial derivative of the ion temperature: $d^2 T_i / d\rho^2$. The dashed line drawn along the 'ridge' in the plot identifies the position of the footpoint of the internal transport barrier.

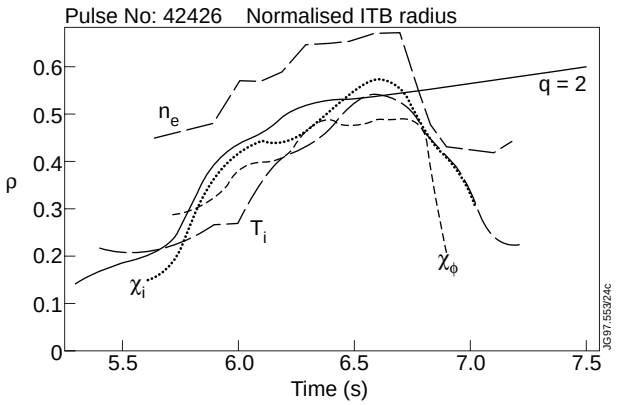

Fig.18. ITB footpoint radii of various quantities.T_i; ion temperature; χ_i : ion thermal diffusivity; χ_ϕ : angular momentum diffusivity, and n_e : electron density. These are plotted with the radius of the q=2 rational surface.

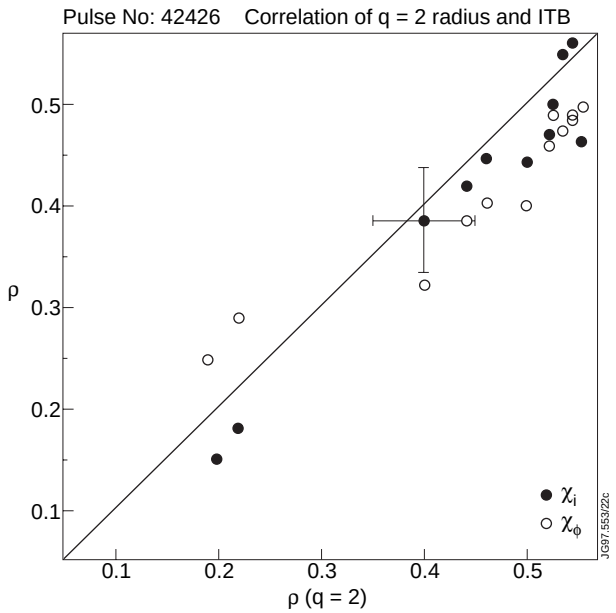

Fig.19. Correlation between the ITB footpoints of the ion thermal diffusivity, χ_i ,(filled circles); and angular momentum diffusivity, χ_ϕ (open circles), with the radius of the q=2 rational surface. Data are shown up to the time of the formation of the H-mode.

4.4 Energy Balance Inside the Internal Transport Barrier

We have investigated the detailed ion and electron energy balances inside the ITB by volume-integration out to the time-varying footpoints of the ITB. Up to the time of the formation of the H-mode, ion channel losses (Fig. 20) were approximately twice those of the electron channel (Fig. 21). Ion and electron conductive losses roughly matched the powers that went into increasing the respective energy contents. As the ion temperature and electron density inside the barrier increased, a significant amount of electron heating power came from equipartition. At time t = 6.6 s, just before the formation of the H-mode, the rate of increase of the ion and electron energy contents began to decrease and this was followed by an increase in the conductive and convective losses in both ion and electron channels. At the time of the H-mode transition, the rate of increase of the ion and electron energy contents inside the barrier region went to zero and thereafter changed sign as the internal transport barrier coexisted with the external H-mode barrier. During the ELM-free H-mode phase, the conductive and convective losses in both channels increased significantly.

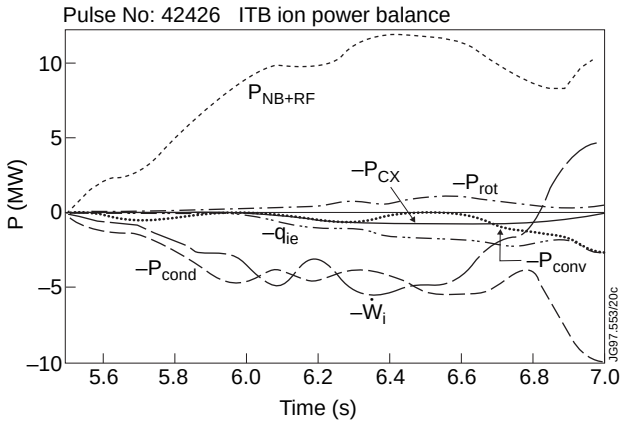

Fig.20. Ion energy balance volume-integrated out to the time-varying ITB radius. P_{NB+RF}: Total ion heating power ; P_{rot}: power to rotation ; $-P_{CX}$: power lost via charge-exchange processes; $-d/dt(W_i)$: power lost to changing the ion thermal energy content; $-P_{cond}$: power lost via conduction; $-P_{conv}$: power lost via convection.

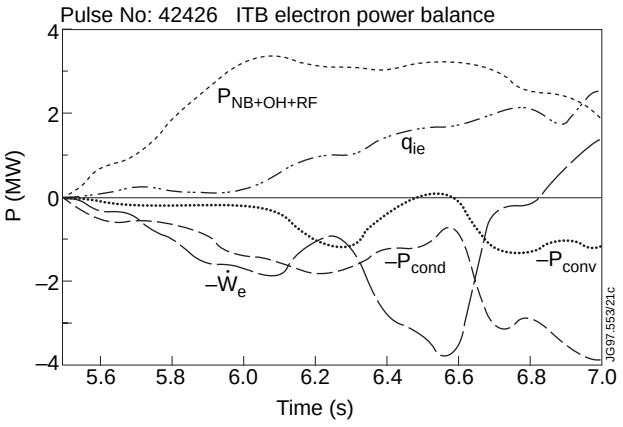

Fig.21. Electron energy balance volume-integrated out to the radius of the ITB. $P_{NB+OH+RF}$: Total electron heating power ; $-q_{ie}$: equipartition power; $d/dt(W_e)$: power lost to changing the electron thermal energy content; $-P_{cond}$: power lost via conduction; $-P_{conv}$: power lost via convection.

4.5 Electron Content within the Internal Transport Barrier

We have investigated the inventory of the total number of electrons deposited (through neutral beam injection) and observed (by density measurements) inside the barrier (Fig. 22). The electron content inside the ITB was determined by volume integration out to its footpoint radius and the time integration started at the formation time of the ITB. The reasonable agreement between the two curves shows that the observed plasma particle inventory in the ITB can be accounted

for by the neutral beam injected particles deposited inside the barrier. Transition of the discharge to the ELM-free H-mode improved the particle confinement at the edge and led to an increase of the total particle inventory.

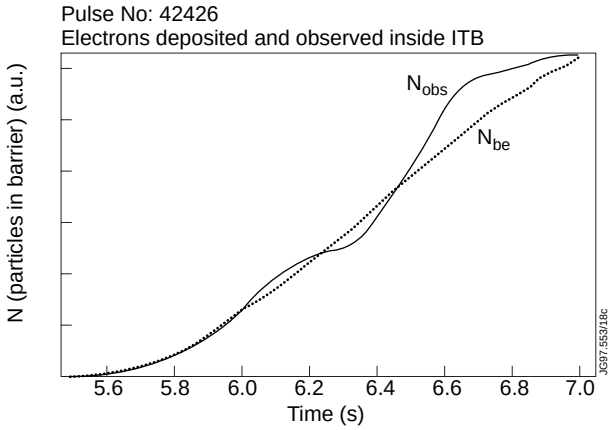

Fig.22. Electron inventory inside the ITB. N_{obs}*: Total number of electrons observed inside the barrier;* N_{be}*: total number of electrons deposited inside the barrier by neutral beam injection.*

5. DISCUSSION AND CONCLUSIONS

If a JET plasma is prepared with an appropriate hollow or weakly sheared central current profile and heated strongly in the centre, an internal transport barrier forms spontaneously. The transport analysis presented here of this optimised shear regime has shown that the ion thermal diffusivity drops by between one and two orders of magnitude to the neo-classical level first in the centre; this is then followed by an expansion phase in which the ITB propagates radially outwards with a velocity ~ 0.5 m s^{-1}.

The growth time of the ITB is considerably longer than that of the formation time of the edge H-mode barrier or the energy confinement time; the evolution of the ITB may be related to the evolution of the magnetic geometry in the plasma core which evolves on a similar time scale (the resistive diffusion time). The correlation between the ITB radius and the radius of the q=2 rational surface is suggestive of a fundamental connection but it must be borne in mind that, in the absence of a diagnostic for the local value of q, the q-profile is not well determined in the centre of the discharge and therefore prone to uncertainty. However, the correlation between the ITB radius and the calculated radius of the q=2 rational surface holds for a number of other high performance optimised shear discharges that have been modelled satisfactorily using TRANSP in the same way.

During the L-mode phase, the temperature and density profiles became increasingly peaked. As the discharge made the transition into the H-mode, the peaked profiles persisted during the ELM-free H-mode period. However, by the time of the H-mode transition, the quality of confinement of the ITB had already begun to degrade (starting in the centre). The highly peaked pressure profiles are susceptible to high frequency MHD instability modes [13] which gradually

degrade the ITB despite control of the additional heating to minimise the effects of the MHD. Another effect may also be significant. The auxiliary power input into the expanding barrier region did not increase in proportion to the plasma volume contained within the barrier, but, as can be seen in Figs. 20 and 21, more slowly than this. Therefore, if there exists, for example, some input power density threshold needed to sustain the barrier then there may not have been enough input power available to sustain it once it had expanded beyond some critical radius.

The H-mode may have been triggered as a result of the enhanced losses from the degrading ITB appearing as extra power fluxes at the plasma edge. This picture is consistent with the sequence of events described above. It must be noted, however, that the power fluxes through the edge were, during the L-mode ITB phase, larger than the steady-current H-mode power threshold. It is possible that the presence of injected edge current density during the plasma-current ramp-up phase raises the steady-state H-mode power threshold; indeed, in experiments where the current ramp was stopped, the H-mode appeared promptly. The NBI power deposited inside the barrier decreased by only ~ 10% at the time the H-mode is triggered owing to the increase in the edge density and the associated NBI power absorption outside the barrier. In view of the smallness of the H-mode edge beam attenuation, it appears unlikely that the barrier degraded solely due to power starvation at the H-mode formation time.

In conclusion, we have observed an improvement in the central confinement in JET with high power heating during the current rise phase of the discharge with a hollow or flat current density profile. When the combined NBI (≤ 20 MW) and ICRH (≤ 6 MW) heating power is increased, a region of reduced transport with highly peaked profiles can result in the L-mode that persists into the later H-mode when the fusion reactivity reaches a maximum. ICRF direct ion heating in the core is efficient with peaked ion temperature and density profiles and was used to control the pressure profile. The clearest signatures of the region of good confinement are large gradients in the ion temperature and toroidal rotation profiles. The position and rate of expansion of the ITB radius correlate well with the calculated position of the rational q=2 surface. The confinement improvement can also be seen in electron density, and, to a lesser extent, in electron temperature, but not necessarily at the same radial region. The ITB can persist in combination with the edge transport barrier characteristics of the H-mode.

ACKNOWLEDGEMENTS

The authors would like to acknowledge the contributions of Task Force P and the specific assistance of D.C.McCune, R.V.Budny, G.Schmidt and M.Zarnstorff from PPPL for their help in using the TRANSP code and of B.Lloyd, C.Warwick and C.Hunt from the Task agreement with the UKAEA.

REFERENCES

[1] Tubbing B. et al, *Nuclear Fusion* **31** (1991), 839.

[2] Hugon, M. et al., *Nuclear Fusion* **32** (1992), 33.

[3] Levington, F.M. et al., *Phys. Rev. Lett.* **75** (1995), 4417.

[4] Strait, E.J. et al., *Phys. Rev. Lett.* **75** (1995), 4421.

[5] Fujita,T. et al., *Plasma Physics and Controlled Nuclear Fusion Research*, Proc. 16th Int. Conf., Montreal, 1996, IAEA-CN-64/A1-4.

[6] Gormezano, C., et al. 1997 *Plasma Physics and Controlled Nuclear Fusion Research*, Proc. 16th Int. Conf., Montreal, 1996, IAEA-CN-64/A5-5.

[7] Sips, A.C.C. et al., Proc. 24th *European Physical Society Conference on Controlled Fusion and Plasma Physics*, Berchtesgaden, Germany, 1997.

[8] Söldner, F.X., et al. Topical Paper. Proc. 24th *European Physical Society Conference on Controlled Fusion and Plasma Physics*, Berchtesgaden, Germany, 1997.

[9] Sips, A.C.C. et al., *Plasma Phys. and Controlled Fusion* (1997)

[10] Goldston, R.J. et al. 1981 *J.Comput.Phys*. **43** 61.

[11] Goldston, R.J. in Basic Processes of Toroidal Fusion Plasmas. 1986 *Proc. Course and Workshop Varenna, 1985.* Vol I, CEC Brussels 165.

[12] Mantsinen M., et al., Proc. 24th *European Physical Society Conference on Controlled Fusion and Plasma Physics*, Berchtesgaden, Germany, 1997.

[13] Huysmans, G.T.A. et al., PProc. 24th *European Physical Society Conference on Controlled Fusion and Plasma Physics*, Berchtesgaden, Germany, 1997.